Chapter 5

Charged Particle Induced Reactions & the Astrophysical p-Process

Understanding proton capture processes on p-nuclei is essential for modeling astrophysical phenomena accurately. Uncertainties in theoretical calculations of these processes impact our models of astrophysical phenomena. We aim to quantify the influence of uncertainties in nuclear model input on reaction cross-sections and reaction rates for proton capture on p-nuclei at astrophysically relevant energies. Utilizing Monte Carlo simulations, we integrate uncertainties related to OMP and NLD parameters. Theoretical calculations are conducted using TALYS- 1.96. Monte Carlo simulations integrate uncertainties by varying input parameters to generate distributions of theoretical outcomes. This study contributes to advancing our comprehension of proton capture processes on p-nuclei and underscores the necessity of rigorous analysis.

This chapter includes research published and forthcoming in peer-reviewed journals:

1. A. Hingu, P.M. Prajapati, et. al., EPJ Web Conf., **275**, 02006, (2023), includes preliminary results. (According to the copyright agreement, the author retains the right to reuse the published work here as a part of this thesis.)

2. A. Hingu, Mahesh Choudhary, K. Katovsky, S. Mukherjee (Submitted in Physica Scripta.)

5.1 Introduction

The study of charged particle-induced reactions is crucial for understanding the nuclear processes underlying astrophysical phenomena, particularly the p-process, which is responsible for producing heavy, proton-rich isotopes in stars. This chapter presents a theoretical investigation of these reactions, with a detailed comparison to experimental data. The astrophysical p-process takes place in the explosive phase of the evolution of massive stars. Such an explosive nucleosynthesis involves a large reaction network. The knowledge of all the relevant reaction rates (calculated from the cross-sections) is essential for the p-process calculations. Despite the recent years' considerable experimental effort, there are still very few cross-sections determined experimentally. In many cases the involved nuclear reactions are not accessible in the laboratory, either due to their low cross-sections or because they involve unstable or exotic isotopes. Thus the p-process calculations are still based mainly on theoretical cross-sections obtained from Hauser Feshbach statistical model calculations.

Theoretical investigation in the case of the p-process is essential due to the extreme conditions and rare occurrences of these reactions in stellar environments, making experimental replication challenging. The p-process involves high temperatures and rapid proton captures and photodisintegration reactions that are difficult to reproduce and measure directly in laboratory settings. Theoretical models allow us to simulate these conditions, predict reaction rates, and understand the nucleosynthesis pathways of heavy, proton-rich isotopes. By comparing these theoretical predictions with available experimental data, we can refine our models, enhance our understanding of stellar processes, and make accurate predictions about the synthesis of elements in the universe.

The isotopes ^{92,94}Mo and ^{74}Se are among the heavy, proton-rich nuclei synthesized during the p-process. Understanding their formation is essential for explaining the observed abundances of these elements in the universe, particularly in old stars and meteorites. In summary, studying the proton capture process on Mo and Se isotopes is crucial for understanding the detailed mechanisms of the p-process, validating theoretical models, and explaining the observed abundances of proton-rich isotopes in the universe.

The aim of our systematic study is to investigate the cross-sections relevant to astrophysical p-process and to check the predictive power of model calculations and this way to put the p-process calculations on a more reliable base.

5.2 Astrophysical Essentials

This section introduces fundamental astrophysical parameters crucial for our analysis. Firstly, we define the reaction rate, which quantifies the speed at which nuclear reactions occur. Next, we elucidate the concept of tunneling through the Coulomb barrier at astrophysical energies, alongside the astrophysical S-factor,

representing the probability of this phenomenon. Additionally, we explore the interaction between the Maxwell-Boltzmann (MB) velocity distribution, depicting nuclear velocities, and the tunneling probability, culminating in the formation of the Gamow peak. This peak signifies the region within stars where nuclear reactions between charged particles predominantly take place. This discussion is grounded in established astrophysical literature, particularly referencing textbooks [1, 2].

5.2.1 Reaction Rate

In stellar plasma, particles move in various directions, driven by the high temperature that imparts thermal motion and kinetic energy to them. When these particles collide, there's a chance for nuclear reactions to occur. The reaction rate, a fundamental quantity in Nuclear Astrophysics, quantifies the number of reactions happening per unit time per unit volume. It hinges on two main factors: the cross-section of the nuclear reaction, representing the probability of reaction occurrence, and the velocity distribution of the particles.

In typical stellar matter, the nondegenerate gas maintains thermal equilibrium. Within this environment, the nuclei exhibit nonrelativistic motion, and their velocity distribution adheres to the widely recognized MB distribution:

$$\mathrm{f_{MB}}(v) = \left(\frac{\mathrm{m}}{2\pi \mathrm{k_B T}}\right)^2 \exp\left(-\frac{\mathrm{m}v^2}{2\mathrm{k_B T}}\right) 4\pi v^2. \tag{5.1}$$

Both species interacting in an environment will have this distribution, so taking velocities for 1 and 2 in the lab-frame.

$$< \sigma v >_{12} = \int_0^\infty \int_0^\infty \mathrm{f_{MB}}(v_1)\, \mathrm{f_{MB}}(v_2)\, \sigma_{12}(v)\, v\, \mathrm{d}v_1\, \mathrm{d}v_2\,, \tag{5.2}$$

where v represents the relative velocity between nuclei 1 and 2. Using the concept of reduced mass:

$$\mu = \frac{\mathrm{m_1 m_2}}{\mathrm{m_1 + m_2}} \tag{5.3}$$

the $< \sigma v >$ can be written as,

$$< \sigma v >_{12} = 4\pi \left(\frac{\mu}{2\pi \mathrm{k_B T}}\right)^{3/2} \int_0^\infty \sigma_{12}(v)\, v \Big(v^2 \exp\left(-\frac{\mu v^2}{2\mathrm{k_B T}}\right)\Big)\, \mathrm{d}v. \tag{5.4}$$

Substituting the center of mass energy $\mathrm{E} = \frac{1}{2}\mu v^2$, we finally arrive at a useful equation for the astrophysical reaction rate per particle pair:

$$< \sigma v >_{12} = \sqrt{\frac{8}{\pi\mu}} \frac{1}{(\mathrm{k_B T})^{3/2}} \int_0^\infty \mathrm{E}\, \sigma_{12}(\mathrm{E}) \exp\left(-\frac{\mathrm{E}}{\mathrm{k_B T}}\right) \mathrm{dE}. \tag{5.5}$$

Here, E represents the center of mass energy, and $\sigma_{12}(\mathrm{E})$ denotes the cross-section of the reaction as a function of energy. This formulation provides a robust equa-

tion for determining the astrophysical reaction rate, crucial for understanding stellar processes.

5.2.2 Reaction Rates for Charged Particle-Induced Reactions

In stars, the nuclear energies involved in interactions are typically insufficient to overcome the formidable potential barriers required for nuclei fusion. However, nuclear fusion processes persist in stars due to the phenomenon of quantum mechanical tunneling. In quantum mechanics, the transmission of particles through a potential barrier is contingent upon the wave function of the incoming particle, whose square magnitude yields the probability distribution of the particle's presence across space. As elucidated in introductory quantum mechanics literature, the wave function for an incoming particle may extend beyond the potential barrier, even when the particle's energy falls below the barrier's height.

In nuclear physics, we investigate the probability of particles tunneling through the repulsive Coulomb barrier. This is modeled using finite barrier potentials encountered by incoming particles. By solving the Schrödinger equation with these potentials, denoted as $\mathrm{V}(\vec{\mathrm{r}})$, we can calculate the transmission coefficient, $\mathcal{T}$. This parameter characterizes the probability of particles penetrating the barrier and entering the nuclear interior. Typically evaluated for charged particles with no angular momentum component (s-wave), $\mathcal{T}$ offers valuable insights into nuclear interactions. which is given by,

$$\mathcal{T} = \mathrm{e}^{-2\pi\eta}, \tag{5.6}$$

where, η denotes Sommerfeld parameter,

$$\eta = \frac{\mathrm{Z_1 Z_2 e^2}}{\hbar}\sqrt{\frac{\mu}{2\mathrm{E}}}. \tag{5.7}$$

In practice the Gamow factor is used,

$$2\pi\eta = 31.29\ \mathrm{Z_1 Z_2}\sqrt{\frac{\mu}{\mathrm{E}}}\,, \tag{5.8}$$

where, μ should be given in amu and centre-of-mass energy E in keV.

5.2.3 The Astrophysical S-factor

The cross-section changes smoothly at higher energies but drops significantly at lower energies due to decreased transmission probability through the Coulomb barrier

$$\sigma(\mathrm{E}) \propto \mathcal{T}. \tag{5.9}$$

Sometimes experimental measurements of cross-sections are unavailable due to this exponential suppression by the Coulomb barrier at low energies. Therefore we measure the cross-section at higher energy and extrapolate it to lower energy.

However, this extrapolation is difficult due to strong energy dependence of the cross-section.

To minimize sensitivity to energy variations in non-resonant reaction, scientists prefer using the astrophysical S-factor for extrapolation instead of cross-sections. This factor is defined as:

$$\mathrm{S(E)} = \frac{\mathrm{E}}{\mathcal{T}}\,\sigma(\mathrm{E}), \tag{5.10}$$

which accounts for all the nuclear effects. The astrophysical S-factor is a rescaled variant of total cross-section $\sigma(\mathrm{E})$ which is essential for many astrophysical applications particularly for the energies below the Coulomb barrier.

This quantity is crucial in astrophysics as it varies smoothly with energy, unlike the cross-section. It allows for safer extrapolations to experimentally inaccessible energies and is also useful for reaction network calculations. Inserting the definition of $\mathrm{S(E)}$ into equation 5.5, the reaction rate per particle pair becomes,

$$< \sigma v >_{12} = \sqrt{\frac{8}{\pi\mu}}\frac{1}{(\mathrm{k_B T})^{3/2}}\int_0^\infty \mathcal{T}\;\mathrm{S(E)}\;\exp\left(-\frac{\mathrm{E}}{\mathrm{k_B T}}\right)\mathrm{dE}, \tag{5.11}$$

inserting equation of $\mathcal{T}$, we obtain:

$$< \sigma v >_{12} = \sqrt{\frac{8}{\pi\mu}}\frac{1}{(\mathrm{k_B T})^{3/2}}\int_0^\infty \exp\left(-\frac{\mathcal{B}}{\sqrt{\mathrm{E}}}\right)\mathrm{S(E)}\;\exp\left(-\frac{\mathrm{E}}{\mathrm{k_B T}}\right)\mathrm{dE}, \tag{5.12}$$

where $\mathcal{B}$ is defined as,

$$\mathcal{B} = \sqrt{2\mu}\pi\,\frac{\mathrm{Z_1 Z_2 e^2}}{\hbar}, \tag{5.13}$$

which correspond to barrier penetrability. The quantity $\mathcal{B}^2$ is called Gamow energy.

5.2.4 The Gamow Window

The combination of the Coulomb penetration probability and the MB velocity distribution gives rise to the phenomenon known as the Gamow peak. This phenomenon, along with the Gamow window, is illustrated in Fig. 5.1. This addresses two scenarios: resonance-free low-energy direct captures and overlapping resonances in high-energy compound reactions, where the cross-section varies smoothly with energy. In stellar environments, nuclear reactions predominantly occur within a narrow energy range around the effective burning energy:

$$\begin{aligned} \mathrm{E_0} &= \left(\frac{\mathcal{B}}{2}\mathrm{k_B T}\right)^{2/3}, \\ \mathrm{E_0} &= 0.12204(\sqrt{\mu}\;\mathrm{Z_1 Z_2 T})^{2/3}\;(\mathrm{MeV}). \end{aligned} \tag{5.14}$$

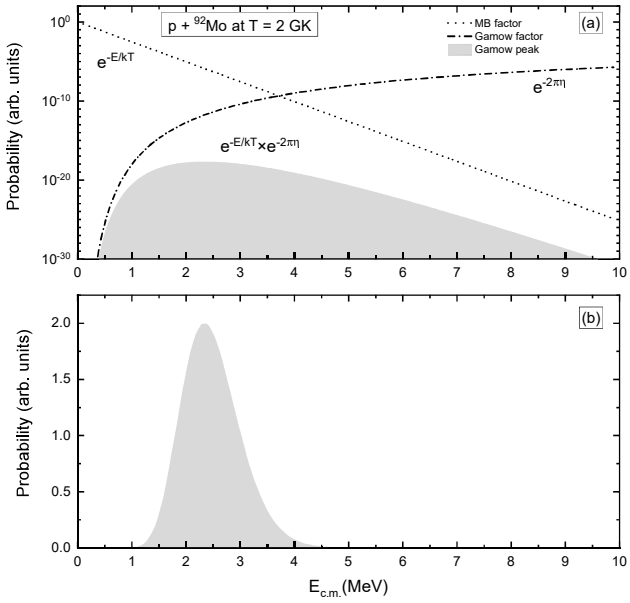

Fig. 5.1: (a) Comparison of MB factor ($\mathrm{e^{-E/kT}}$; dotted line) and Gamow factor ($\mathrm{e^{-2\pi\eta}}$; dashhed-dotted line) versus energy for $^{92}\mathrm{Mo(p,\gamma)^{93}Tc}$ reaction at T= 2 GK. The product $\mathrm{e^{-E/kT}e^{-2\pi\eta}}$ is referred to as Gamow peak is shown in shaded region, (b) The same Gamow peak is shown on a linear scale.

This equation suggests that with an increase in both the charge numbers and stellar temperature, the Gamow peak shifts towards higher energy. The effective width $\Delta \mathrm{E_0}$ of the energy window can be defined as,

$$\Delta \mathrm{E_0} = 0.23682(\mu\ \mathrm{Z_1^2 Z_2^2 T^5})^{1/6}\ (\mathrm{MeV}). \tag{5.15}$$

Here T is the plasma temperature in gigakelvins (GK), Eqs. 5.14 and 5.15 are widely used to determine a relevant energy range $\mathrm{E_0 - (\Delta E_0/2)} \leq \mathrm{E} \leq \mathrm{E_0 + (\Delta E_0/2)}$ within which the nuclear cross-sections have to be known. This region represents the effective energy window for non-resonant thermonuclear reactions in stars which is shown in Fig. 5.1.

Fig. 5.1 illustrates the significance of the Gamow window for $\mathrm{p} + ^{92}\mathrm{Mo}$ at T = 2 GK. The logarithmic scale highlights the small magnitude of the integrand $\mathrm{e^{-E/kT}e^{-2\pi\eta}}$ compared to the Gamow and MB factors. Despite its narrowness, the Gamow window represents the energy range where nuclear reactions are most effective. The variation of Gamow peak energy and Gamow peak width with temperature for $\mathrm{p} + ^{92}\mathrm{Mo}$ is shown in Fig. 5.2.

The main challenge in nuclear astrophysics is to determine the cross-sections within the Gamow window or in its proximity. This chapter endeavors to investigate proton-induced reactions on Mo and Se isotopes at energies relevant to the p-process.

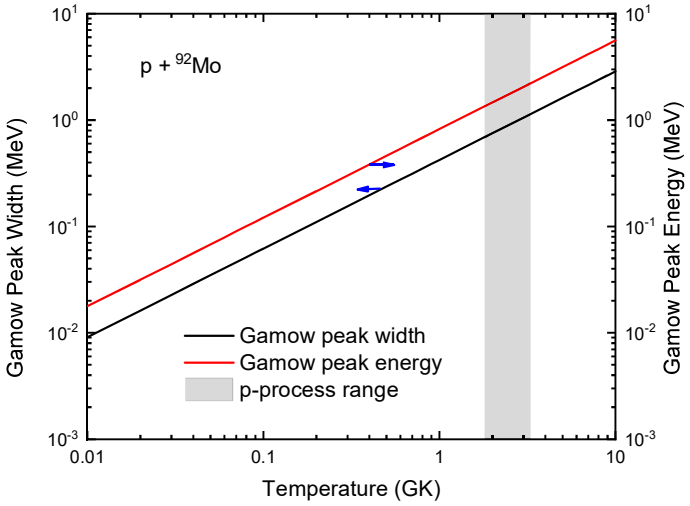

Fig. 5.2: Variation of Gamow peak width and energy with respect to temperature for the case of $\mathrm{p} + {}^{92}\mathrm{Mo}$. Shaded region shows the temperature range for p-process.

5.2.5 The Astrophysical p-Process

The astrophysical p-process, responsible for the synthesis of proton-rich isotopes in stars, stands as one of the least explored phenomena in nucleosynthesis. A significant portion of elements heavier than iron are produced through successive neutron capture processes, namely the s-process and/or r-processes. However, 35 nuclei located on the proton-rich side of the stability valley cannot be formed through neutron capture, as their pathways are blocked by stable isotopes [3, 4]. Here, we present an overview of these nuclei, commonly referred to as the p-nuclei, and their synthesis process known as the p-process.

The p-Nuclei

p-Nuclei production is mainly attributed to the p-process, which involves the synthesis of proton-rich nuclei through two primary mechanisms: proton capture on lighter seed nuclei, including reactions such as (p, γ) and (p, n), and photonuclear reactions on heavier, stable nuclides, such as (γ, n), (γ, p), and (γ, α) [5].

p-Process Sites

The astrophysical site(s) where the p-process occurs have not yet been clearly identified [6]. To accurately model the natural abundances of the p-isotopes, p-process models require a comprehensive nuclear reaction network. A precise understanding of the rates of nuclear reactions within this network is essential for reliable abundance calculations and for identifying the astrophysical site(s) involved. Some proposed sites for the p-process include Type II supernovae (SNII) [7] and Type Ia supernovae [8]. For decades, SNII have been the preferred

site for the p-process, especially when the shock wave passes through the O/Ne layer of the star, where temperatures relevant to the p-process (ranging from 1.8 to 3.3 GK) are reached. However, recent studies propose that the Type Ia scenario may play a more significant role in the abundances of p-nuclei [9]. Moreover, the νp-process in neutrino-driven winds of SNII is also thought to contribute to the production of p-nuclei [10].

5.3 Proton Capture Reactions of Mo & Se Isotopes

To completely determine the nucleosynthesis of p-process, accurate knowledge of capture and photo-disintegration reaction rates for about 3000 stable and proton-rich nuclei is essential. However, due to the low cross-sections encountered, experimental data on proton reactions are scarce at low energies in the mass region relevant to the γ-process. Experimental data started to accumulate only in the last 20 years. Still, the number of studied reactions remains relatively small compared to the huge number of reactions involved in a γ-process network [11]. For the reactions whose experimental data are not available yet, the state-of-the-art nuclear reaction models and the nuclear structure knowledge deduced by microscopic models should be taken into account for the evaluations of reaction rates. There are two different methods for cross-section measurements: the in-beam γ-detection technique and activation which can be used to determine the cross-section accurately.

In the present study, we perform the systematic computations of (p,γ) reaction cross-section on Mo and Se isotopes based on the TALYS software [12]. We have also calculated the S-factor for each case as well. The present results are also compared with the previous experimental data from EXFOR database [13]. The basis of the new p-process database is the Experimental Nuclear Reaction Data (EXFOR) database, which has the advantage that it contains (almost) all available experimental cross-sections and is regularly updated. However, it contains also a lot of irrelevant data for the p-process, because most measurements were performed far away from the Gamow window and have no astrophysical importance. Therefore we restrict our data to energies of maximum 1.5 times the upper end of the Gamow window at 3 GK for the respective reactions. This upper cut-off energy was arbitrarily chosen because most available data was measured above the astrophysically important Gamow windows, which lie (for T=3 GK) between E=3 and 6 MeV for proton-induced reactions [14].

The subsequent sections address the parameterization of the OMP and NLD, alongside the application of the Monte Carlo method to assess uncertainties in theoretical predictions using the TALYS code.

5.3.1 OMP Parameterization

The phenomenological, OMP for nucleon–nucleus scattering, denoted as $\mathcal{U}$, is generally expressed as [15]:

$$\begin{aligned}\mathcal{U}(\mathrm{r},\mathrm{E}) = &-\mathcal{V}_{\mathrm{V}}(\mathrm{r},\mathrm{E}) - \mathrm{i}\mathcal{W}_{\mathrm{V}}(\mathrm{r},\mathrm{E}) - \mathrm{i}\mathcal{W}_{\mathrm{D}}(\mathrm{r},\mathrm{E}) + \mathcal{V}_{\mathrm{SO}}(\mathrm{r},\mathrm{E}).\mathrm{l}.\sigma \\ &+ \mathrm{i}\mathcal{W}_{\mathrm{SO}}(\mathrm{r},\mathrm{E}).\mathrm{l}.\sigma + \mathcal{V}_{\mathrm{C}}(\mathrm{r})\end{aligned} \tag{5.16}$$

Here, $\mathcal{V}_{\mathrm{V}}, \mathcal{V}_{\mathrm{SO}}$ and $\mathcal{W}_{\mathrm{V}}, \mathcal{W}_{\mathrm{D}}, \mathcal{W}_{\mathrm{SO}}$ represent the real and imaginary parts of the volume-central (V), surface-central (D), and spin-orbit (SO) potentials, respectively. E denotes the laboratory energy of the incident particle, measured in MeV. All components are categorized into energy-dependent well depths, $\mathcal{V}_{\mathrm{V}}, \mathcal{W}_{\mathrm{V}}, \mathcal{W}_{\mathrm{D}}, \mathcal{V}_{\mathrm{SO}}$, and $\mathcal{W}_{\mathrm{SO}}$, as well as energy-independent radial functions f.

$$\begin{aligned}\mathcal{V}_{\mathrm{V}}(\mathrm{r},\mathrm{E}) &= \mathrm{V}_{\mathrm{V}}(\mathrm{E})\mathrm{f}(\mathrm{r},\mathrm{R}_{\mathrm{V}},\mathrm{a}_{\mathrm{V}}), \\ \mathcal{W}_{\mathrm{V}}(\mathrm{r},\mathrm{E}) &= \mathrm{W}_{\mathrm{V}}(\mathrm{E})\mathrm{f}(\mathrm{r},\mathrm{R}_{\mathrm{V}},\mathrm{a}_{\mathrm{V}}), \\ \mathcal{W}_{\mathrm{D}}(\mathrm{r},\mathrm{E}) &= -4\mathrm{a}_{\mathrm{D}}\mathrm{W}_{\mathrm{D}}(\mathrm{E})\frac{\mathrm{d}}{\mathrm{dr}}\mathrm{f}(\mathrm{r},\mathrm{R}_{\mathrm{D}},\mathrm{a}_{\mathrm{D}}), \\ \mathcal{V}_{\mathrm{SO}}(\mathrm{r},\mathrm{E}) &= \mathrm{V}_{\mathrm{SO}}(\mathrm{E})\Big(\frac{\hbar}{\mathrm{m}_{\pi}\mathrm{c}}\Big)^2\frac{1}{\mathrm{r}}\frac{\mathrm{d}}{\mathrm{dr}}\mathrm{f}(\mathrm{r},\mathrm{R}_{\mathrm{SO}},\mathrm{a}_{\mathrm{SO}}), \\ \mathcal{W}_{\mathrm{SO}}(\mathrm{r},\mathrm{E}) &= \mathrm{W}_{\mathrm{SO}}(\mathrm{E})\Big(\frac{\hbar}{\mathrm{m}_{\pi}\mathrm{c}}\Big)^2\frac{1}{\mathrm{r}}\frac{\mathrm{d}}{\mathrm{dr}}\mathrm{f}(\mathrm{r},\mathrm{R}_{\mathrm{SO}},\mathrm{a}_{\mathrm{SO}}).\end{aligned} \tag{5.17}$$

The form factor $\mathrm{f}(\mathrm{r},\mathrm{R}_{\mathrm{i}},\mathrm{a}_{\mathrm{i}})$ is represented by a Woods-Saxon distribution, which is defined as follows:

$$\mathrm{f}(\mathrm{r},\mathrm{R}_{\mathrm{i}},\mathrm{a}_{\mathrm{i}}) = \frac{1}{1+\exp\left[\frac{(\mathrm{r}-\mathrm{R}_{\mathrm{i}})}{\mathrm{a}_{\mathrm{i}}}\right]}, \tag{5.18}$$

where A is the atomic mass number, with geometric parameters defined as the radius $\mathrm{R}_{\mathrm{i}} = \mathrm{r}_{\mathrm{i}}\mathrm{A}^{1/3}$ and the diffuseness parameters a_{i}. For charged projectiles, the Coulomb potential $\mathcal{V}_{\mathrm{C}}$ is represented by the potential of a uniformly charged sphere:

$$\begin{aligned}\mathcal{V}_{\mathrm{C}}(\mathrm{r}) &= \frac{\mathrm{Zze}^2}{2\mathrm{R}_{\mathrm{C}}}\Big(3-\frac{\mathrm{r}^2}{\mathrm{R}_{\mathrm{C}}^2}\Big), \text{for } \mathrm{r} \le \mathrm{R}_{\mathrm{C}}, \\ &= \frac{\mathrm{Zze}^2}{\mathrm{r}}, \text{for } \mathrm{r} \ge \mathrm{R}_{\mathrm{C}},\end{aligned} \tag{5.19}$$

here $\mathrm{Z}(\mathrm{z})$ indicates the charge of the target or projectile, while $\mathrm{R}_{\mathrm{C}} = \mathrm{r}_{\mathrm{C}}\ \mathrm{A}^{1/3}$ signifies the Coulomb radius.

The potential depths are characterized by the term $\mathrm{E}-\mathrm{E}_{\mathrm{f}}$, where E_{f} is the Fermi energy in MeV, defined as the energy level situated between the last occupied shell and the first unoccupied shell of the nucleus. For incident protons,

the Fermi energy is given by:

$$E_f^p = -\frac{1}{2}[S_p(Z,N) + S_p(Z+1,N)], \tag{5.20}$$

where S_p denotes the proton separation energies for a nucleus characterized by number Z and neutron number N.

The global proton OMP is given by:

$$\begin{aligned}
V_V(E) &= v_1[1 - v_2(E - E_f^p) + v_3(E - E_f^p)^2 - v_4(E - E_f^p)^3] \\
&\quad + \bar{V}_C\, v_1[v_2 - 2v_3(E - E_f^p) + 3v_4(E - E_f)^2]\,, \\
W_V(E) &= w_1 \frac{(E - E_f^p)^2}{(E - E_f^p)^2 + (w_2)^2}\,, \\
r_V &= 1.3039 - 0.4054\ A^{-1/3}\,, \\
a_V &= 0.6778 - 1.487 \times 10^{-4}\ A\,, \\
W_D(E) &= d_1 \frac{(E - E_f^p)^2}{(E - E_f^p)^2 + (d_3)^2} \exp[-d_2(E - E_f^p)]\,, \\
r_D &= 1.3424 - 0.01585\ A^{1/3}\,, \\
a_D &= 0.5187 + 5.205 \times 10^{-4} A\,, \\
V_{SO}(E) &= v_{so1} \exp[-v_{so2}(E - E_f^p)]\,, \\
W_{SO}(E) &= w_{so1} \frac{(E - E_f^p)^2}{(E - E_f^p)^2 + (w_{so2})^2}\,, \\
r_{SO} &= 1.1854 - 0.647\ A^{-1/3}\,, \\
a_{SO} &= 0.59\,, \\
r_C &= 1.198 + 0.697\ A^{-2/3} + 12.994\ A^{-5/3}\,,
\end{aligned} \tag{5.21}$$

where the parameters for the potential depths, $\bar{V}_C$ and E_f^p are given as:

$$\begin{aligned}
\bar{V} &= 1.73\ Z\ A^{-1/3}/r_C\,, \\
E_f^p &= -8.4075 + 0.01378\ A.
\end{aligned} \tag{5.22}$$

The optical model parameters r_V, a_V, v_1, v_2, v_3, w_1, w_2, r_D, a_D, d_1, d_2, d_3, r_{SO}, a_{SO}, v_{SO1}, v_{SO2}, w_{SO1}, and w_{SO2} are employed to quantify the uncertainties in theoretical predictions.

5.3.2 NLD Parameterization

Nuclear level density is a key factor in the determination of reaction cross sections, as it governs the distribution of available nuclear energy states with respect to excitation energy. This distribution directly influences the population of excited states within compound nuclei, thereby affecting the resulting reaction cross section. The total level density within the Fermi gas model at excitation energy E_x is described by the following equation [16]:

$$\rho_{\mathrm{FG}}^{\mathrm{tot}}(\mathrm{E_{exc}}) = \frac{1}{\sqrt{2\pi}\sigma}\frac{\sqrt{\pi}}{12}\frac{\exp(2\sqrt{\mathrm{aU}})}{\mathrm{a}^{1/4}\ \mathrm{U}^{5/4}}, \tag{5.23}$$

where the effective excitation energy is given by:

$$\mathrm{U} = \mathrm{E_{exc}} - \Delta. \tag{5.24}$$

Here, Δ is the energy shift parameter, typically tuned to replicate the odd-even staggering observed in experimental nuclear mass data. The energy shift is given by the equation $\Delta = \chi\frac{12}{\sqrt{\mathrm{A}}} + \delta$, where χ takes the value of -1 for odd-odd nuclei, 1 for even-even nuclei, and 0 for odd-even nuclei. The parameter δ is adjustable to optimize the fit with experimental data. In Eq. (5.23), the parameters a and σ denote the level density parameter and the spin cut-off parameter, respectively. The level density parameter (a) is defined as:

$$\mathrm{a}(\mathrm{E_{exc}}) = \tilde{\mathrm{a}}\Big(1 + \delta\mathrm{W}\frac{1-\exp(-\gamma\mathrm{U})}{\mathrm{U}}\Big), \tag{5.25}$$

where $\tilde{\mathrm{a}}$ represents the asymptotic level density, expressed as:

$$\tilde{\mathrm{a}} = \alpha\mathrm{A} + \beta\mathrm{A}^{2/3}. \tag{5.26}$$

with A being the mass number. The damping factor (γ) is systematically determined by the relation:

$$\gamma = \frac{\gamma_1}{\mathrm{A}^{1/3}}. \tag{5.27}$$

The level density parameters σ, α, β, and γ in conjunction with the previously defined OMP parameters (Section 5.3.1), are utilized to evaluate uncertainties in theoretical predictions.

5.3.3 Uncertainty Quantification Using Monte Carlo Method

In this study, we assume that each nuclear model parameter possesses its own uncertainty. To evaluate the uncertainties in theoretically calculated cross-sections and reaction rates for proton capture reactions on p-nuclei, we employed the Monte Carlo Method. We specifically focus on the systematic variation of two key nuclear inputs: the OMP and the NLD parameter. These inputs are fundamental for theoretical models to accurately depict nuclear reaction mechanisms and energy-dependent cross-sections. Another crucial factor in determining the nuclear reaction cross-section is the level density. It describes how the density of nuclear energy levels varies with excitation energy, impacting the population of excited states in compound nuclei and, in turn, the reaction cross-section. Theoretical calculations of nuclear reaction cross-sections are associated with various uncertainties. These uncertainties can originate from various sources, including uncertainty in the model parameters, inherent flaws in the models,

Table 5.1: Details of proton OMP parameters used in the present work, along with their corresponding values for Z=42 and A=92, and the associated percentage uncertainties [18, 19].

OMP Parameter	Value	Unit	Uncertainty (%)
$r_V = 1.3039 - 0.4054\ A^{-1/3}$	1.214097629	fm	2
$a_V = 0.6778 - 0.0001487\ A$	0.6641196	MeV	2
$v_1 = 59.3 + 21(N-Z)/A - 0.024\ A$	58.91808696	MeV	2
$v_2 = 0.007067 + 4.23 \times 10^{-6}\ A$	0.00745676	MeV^{-1}	3
$v_3 = 1.729 \times 10^{-5} + 1.136 \times 10^{-8}\ A$	0.000018335	MeV^{-3}	3
$w_1 = 14.667 + 0.009629\ A$	15.552868	MeV	10
$w_2 = 73.55 + 0.0795\ A$	80.864	MeV	10
$r_D = 1.3424 - 0.01585\ A^{1/3}$	1.33888898	fm	3
$a_D = 0.5187 + 0.0005205\ A$	0.5293648	MeV	4
$d_1 = 16 + 16(N-Z)/A$	17.39130435	MeV	10
$d_2 = 0.0180 + 0.003802/(1 + \exp[(A-156)/8)]$	0.021800725	MeV^{-1}	10
$d_3 = 11.5$	11.5	MeV	10
$r_{SO} = 1.1854 - 0.647\ A^{-1/3}$	1.042079492	fm	10
$a_{SO} = 0.59$	0.59	MeV	10
$v_{so1} = 5.922 + 0.003\ A$	6.198	MeV	5
$v_{so2} = 0.0040$	0.004	MeV^{-1}	10
$w_{so1} = -3.1$	3.1	MeV	20
$w_{so2} = 160$	160	MeV	20

and errors in algorithms, among others. [17, 18]. Therefore, a quantitative knowledge of these sources of uncertainty and their impact on the model's final results is crucial. A popular Woods-Saxon phenomenological OMP parameters were used in our calculation. To account for the potential variations arising from uncertainties in both the OMP and NLD parameters, we adopt the Monte Carlo Method [18–20]. The main purpose of the Monte Carlo Method is to understand how uncertainties in the nuclear model and level density parameters affect the final reaction cross-section. This method involves exploring a range of possible parameter values within their known uncertainty ranges. By running numerous simulations (100 in this case) in the TALYS nuclear code [19, 21] with these varied parameter sets, we generate a distribution of reaction cross-sections. This distribution essentially reveals the impact of these uncertainties on the final results. The initial parameters employed in this study are the global level density parameters introduced by A. J. Koning et al. [16] and the OMP parameters proposed by Koning and Delaroche [15]. Furthermore, we used the initial parameter uncertainties from Reference [19] to include uncertainties into our study. The OMP parameters for protons, along with their corresponding values for Z=42 and A=92, and the percentage uncertainties are shown in 5.1, based on the approaches of Koning et al. [18, 19]. Table 5.2 presents the NLD parameters, and the corresponding percentage uncertainties applied for Z=42 and A=92.

Table 5.2: Details NLD parameters and their associated percentage uncertainties used in the present work for Z=42 and A=92 [18, 19].

Level Density Parameter	Value	Uncertainty (%)
σ^2	1.192	30
α	0.0722396	20
β	0.195267	30
γ	0.410289	30

5.3.4 Calculations

This study involves performing a detailed uncertainty quantification of proton OMP and NLD parameters through Monte Carlo simulations and using the TALYS nuclear reaction code to compute both reaction cross-sections and reaction rates. By sampling the parameters from a multivariate normal distribution, considering their uncertainties and correlations, we generate multiple parameter sets. Each set is used to run TALYS, which calculates the corresponding nuclear reaction cross-sections and reaction rates. From the ensemble of cross-sections obtained, we calculate the mean cross-sections and their covariance matrix. The mean cross-sections $\bar{\sigma}$ are calculated as:

$$\bar{\sigma} = \frac{1}{N}\sum_{i=1}^{N}\sigma_i, \tag{5.28}$$

where N is the number of Monte Carlo samples, and σ_i represents the cross-section obtained from the i^{th} TALYS run. The covariance matrix Cov_σ of the cross-sections is derived as:

$$\mathrm{Cov}_{\sigma(i,j)} = \frac{1}{N}\sum_{k=1}^{N}(\sigma_{ik}-\bar{\sigma}_i)(\sigma_{jk}-\bar{\sigma}_j). \tag{5.29}$$

Similarly, the reaction rates $\bar{R}$ and their covariance matrix Cov_R are computed using the same approach:

$$\bar{R} = \frac{1}{N}\sum_{i=1}^{N}R_i, \tag{5.30}$$

$$\mathrm{Cov}_{R(i,j)} = \frac{1}{N}\sum_{k=1}^{N}(R_{ik}-\bar{R}_i)(R_{jk}-\bar{R}_j). \tag{5.31}$$

This approach allows us to derive the standard deviations (uncertainties) of the cross-sections and reaction rates, $\sqrt{\mathrm{Cov}_{\sigma(i,i)}}$ and $\sqrt{\mathrm{Cov}_{R(i,i)}}$, thereby providing a comprehensive understanding of how uncertainties in the input parameters propagate through to the predicted quantities. The results elucidate the variability and reliability of the calculated cross-sections and reaction rates, offering critical insights for nuclear data evaluations and their applications in nuclear

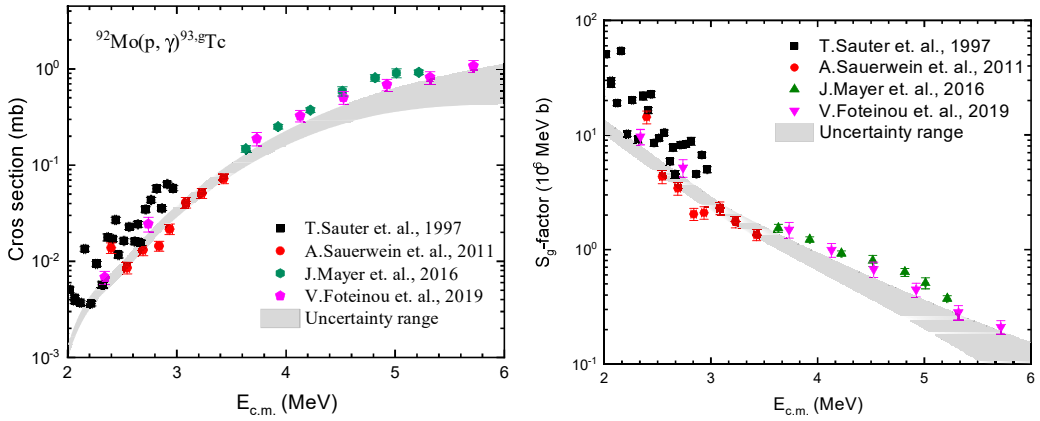

Fig. 5.3: Cross-section and S-factor for the ^{92}Mo(p,γ)^{93g}Tc reaction calculated using TALYS, compared with experimental data from EXFOR [22–25].

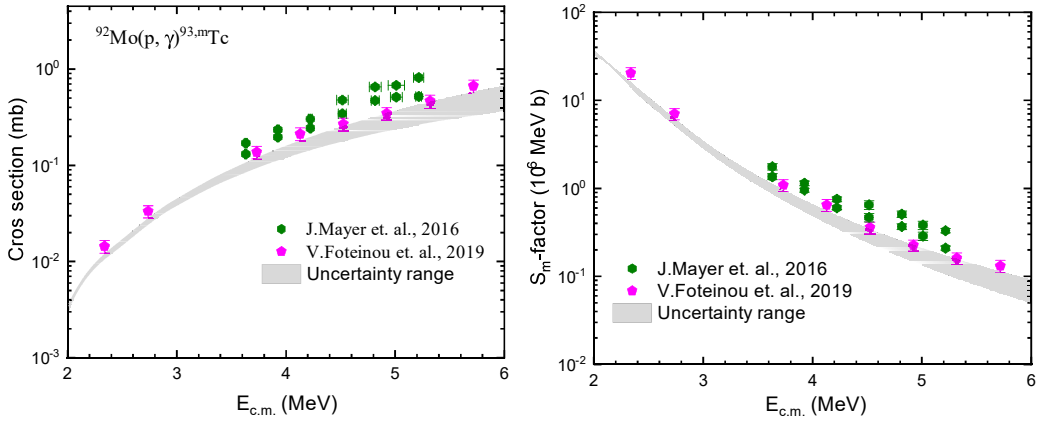

Fig. 5.4: Cross-section and S-factor for the ^{92}Mo(p,γ)^{93m}Tc reaction calculated using TALYS, compared with experimental data from EXFOR [24, 25].

physics and astrophysics.

5.4 Results and Discussion

A comparison between the existing experimental data from EXFOR [30] and theoretical predictions for the reaction cross-section & S-factor for reaction ^{92}Mo(p,γ)^{93,g}Tc, ^{92}Mo(p,γ)^{93,m}Tc, ^{94}Mo(p,γ)^{95,g}Tc, ^{74}Se(p,γ)^{75}Br, ^{76}Se(p,γ)^{77}Br and, ^{82}Se(p, n)^{82}Br are presented in Figs. 5.3, 5.4, 5.5, 5.6, 5.7 and, 5.8 respectively. The results from A. Sauerwein et al. [23] and V. Foteinou et al. [25] show good agreement with the theoretical predictions. In contrast, the data from T. Sauter et al. [22] and J. Mayer et al. [24] tend to overestimate the cross-section values for ^{92}Mo(p,γ)^{93,g}Co. Specifically, V. Foteinou et al. [25] provide data consistent with theoretical models, whereas J. Mayer et al. report higher than expected

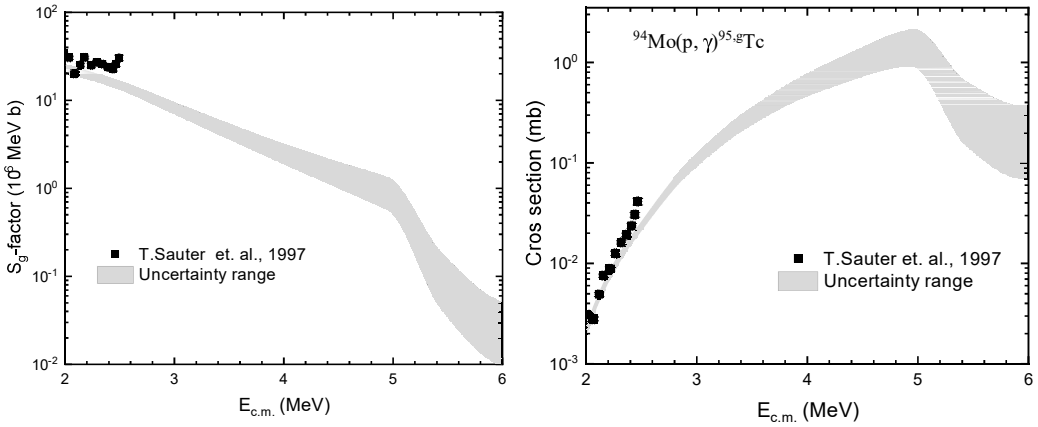

Fig. 5.5: Cross-section and S-factor for the ^{94}Mo(p,γ)^{95,g}Tc reaction calculated using TALYS, compared with experimental data from EXFOR [24, 25].

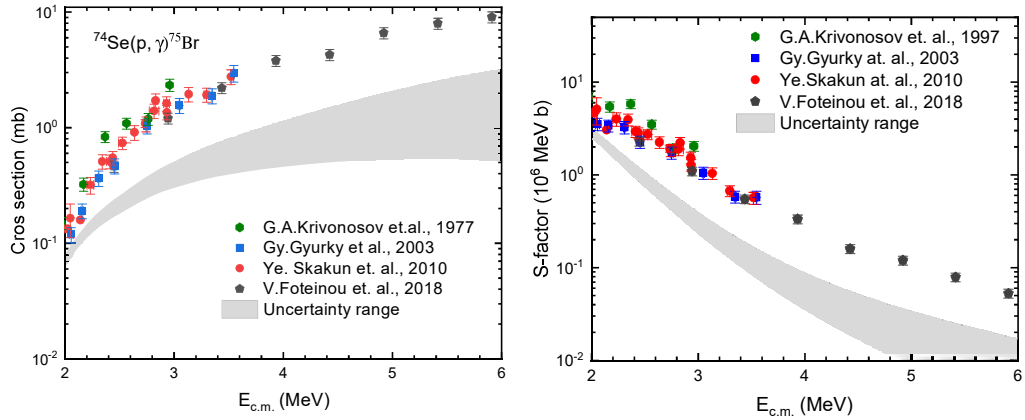

Fig. 5.6: Cross-section and S-factor for the ^{74}Se(p, γ)^{75}Br reaction calculated using TALYS, compared with experimental data from EXFOR [26–29].

cross-section values for ^{92}Mo(p,γ)^{93,m}Co. The results of T. Sauter et al. [22] agree well with theoretical predictions for the ^{94}Mo(p,γ)^{95,g}Tc reaction, also indicating a lack of data points above 2.5 MeV, thereby highlighting an area for further experimental investigation [31]. For the ^{74}Se(p,γ)^{75}Br reaction, a notable discrepancy exists between experimental data and theoretical predictions, with experimental measurements overestimating the reaction cross-sections compared to the theoretical models. For the ^{76}Se(p,γ)^{77}Br reaction, results from Gy. Gyrurky et al. [28] align with theoretical predictions up to 2.25 MeV, beyond which the predictions are consistently underestimating the experimental data. Similarly, results from Ye. Skakun et al. [27] align with theoretical predictions up to 2.5 MeV, beyond which the predictions are consistently underestimating the experimental data. For the reaction ^{82}Se(p, n)^{82}Br, recent experimental results show good agreement with theoretical predictions. Simulated reaction rates for ^{92}Mo(p,γ)^{93}Tc, ^{94}Mo(p,γ)^{95}Tc, ^{74}Se(p,γ)^{75}Br, and , ^{76}Se(p,γ)^{77}Br are depicted in

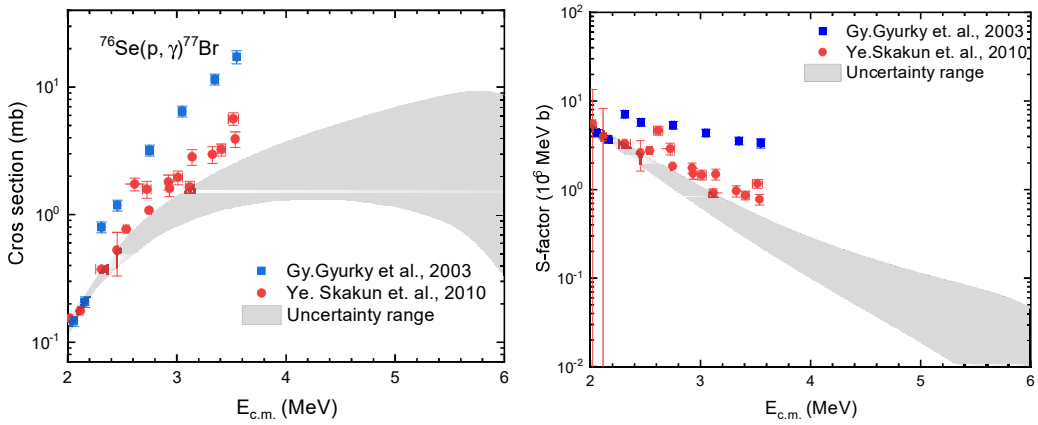

Fig. 5.7: Cross-section and S-factor for the ^{76}Se(p, γ)^{77}Br reaction calculated using TALYS, compared with experimental data from EXFOR [27, 28].

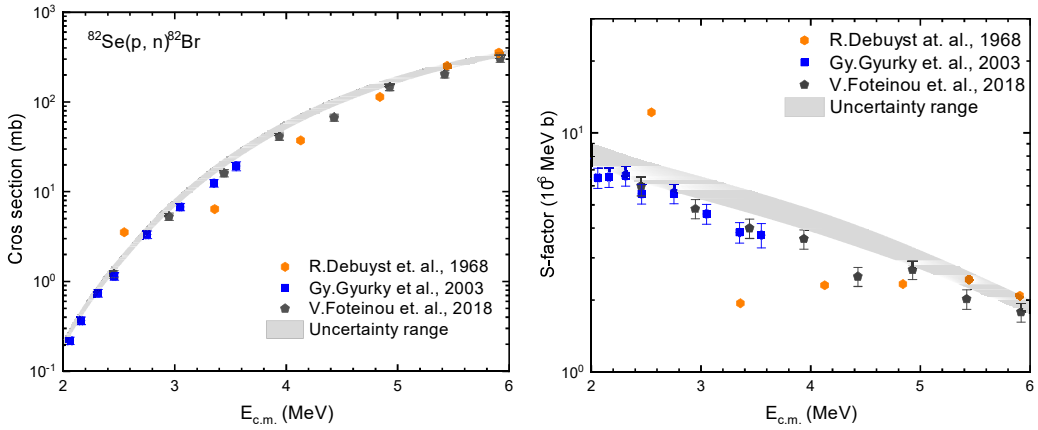

Fig. 5.8: Cross-section and S-factor for the ^{82}Se(p, n)^{82}Br reaction calculated using TALYS, compared with experimental data from EXFOR [26, 28, 35].

Figs. 5.9, 5.10, 5.11, and, 5.12 respectively. The reaction products are radioactive and the activation method [32, 33] as discussed in Chapter 3 can be used to determine the cross section. Theoretical prediction or systematic approach [34] and indirect methods as well can be useful where reaction cross section is not directly possible to measure. Gathering new, independent data on Woods-Saxon OMP parameters and NLDs is essential for refining and improving global nuclear models.

5.5 Summary and Conclusions

In this study, we have presented a comprehensive analysis of the uncertainty quantification for proton capture on selected heavy proton rich nuclei (^{92,94}Mo and ^{74,76}Se). The impact of the uncertainties associated with OMP parameters

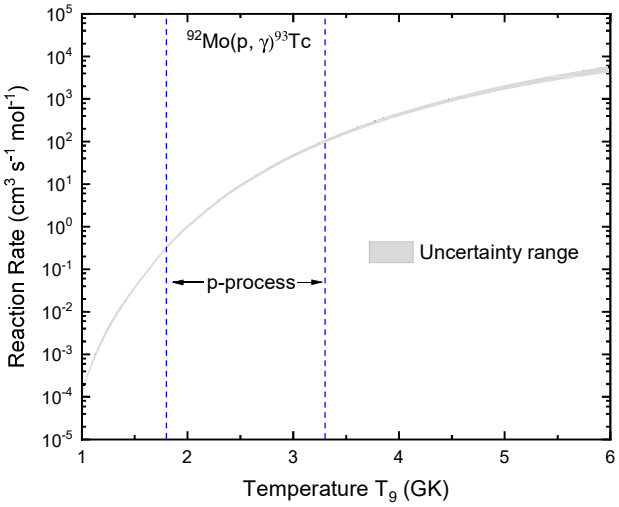

Fig. 5.9: Theoretically simulated reaction rate for ^{92}Mo(p,γ)^{93}Tc reaction.

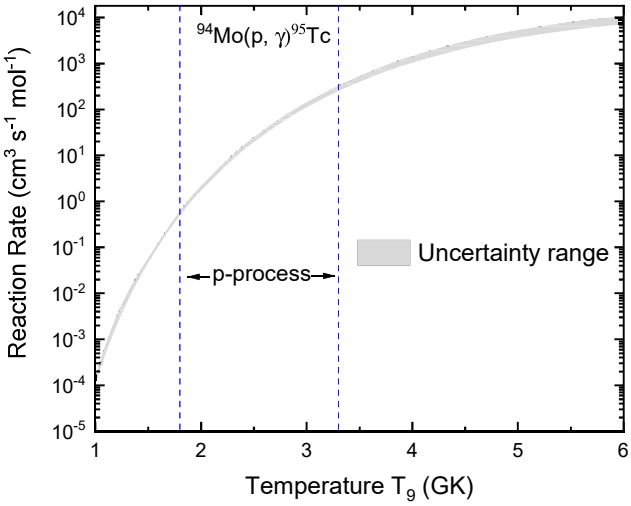

Fig. 5.10: Theoretically simulated reaction rate for ^{94}Mo(p,γ)^{95}Tc reaction.

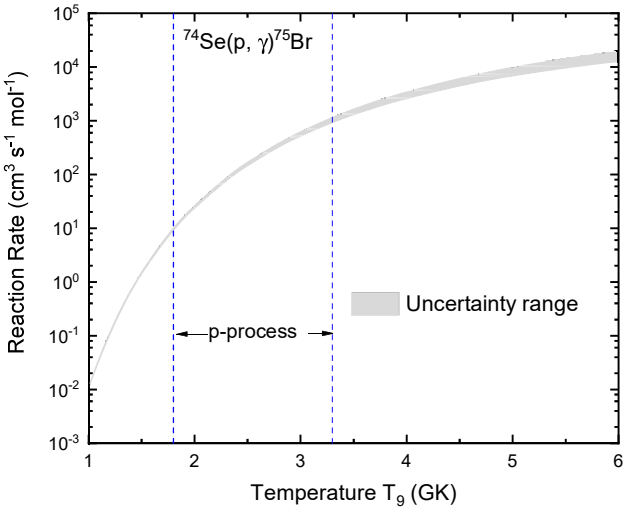

Fig. 5.11: Theoretically simulated reaction rate for ^{74}Se(p,γ)^{75}Br reaction.

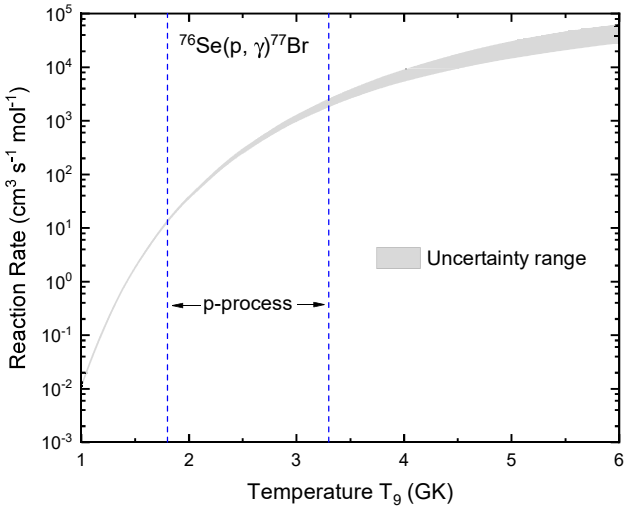

Fig. 5.12: Theoretically simulated reaction rate for ^{74}Se(p,γ)^{75}Br reaction.

and NLD parameters on the predictions for proton capture reactions at astrophysically relevant energies were systematically investigated using the Monte Carlo method. Accurately understanding proton capture processes at these energies is crucial for (a) assessing the validity of Woods-Saxon phenomenological OMP parameters and NLD parameters in cross-section calculations, and (b) evaluating how uncertainties in these models propagate into reaction rates, which are fundamental for precise abundance predictions. Our findings indicate that most experimentally measured cross-sections from EXFOR library are consistent within the theoretical uncertainty bands. Understanding proton capture processes at these energies is crucial for elucidating nucleosynthesis in stellar environments, particularly in the p-process, which produces proton-rich isotopes. This research enhances the reliability of nuclear reaction models used in astrophysical applications by providing a detailed uncertainty analysis, contributing to a better understanding of the origins and abundances of elements in the universe.

Summarizing the available data for studying explosive burning it becomes apparent that, experimental data close to astrophysically relevant energies are very scarce. Although, as discussed in section 5.2.4, high-temperature environments severely limit the possibility to directly determine astrophysical reactivities, there is an urgent need to experimentally cover the relevant energy range to obtain data for the improvement of the theoretical predictions. Given the shortcomings and diversity of processes suggested for the production of p-nuclei (Section 5.2.5), a reliable database and reliable predictions are needed as a firm basis for future investigations. The accurate knowledge of reaction rates or, at least, their realistic uncertainties may allow to rule out certain astrophysical models on the grounds of nuclear physics considerations.

Certainly, further investigation is required in this region of the nuclear chart, both theoretically and experimentally, to provide firm insight at the driving mechanisms behind the p-process reaction network, as well as to improve the phenomenological parts of the OMPs in an energy region where a scarcity of experimental data, even for stable nuclei, still persists. The acquisition of new, independent data on OMPs and NLDs is crucial for refining global nuclear models. OMPs describe the interactions between projectiles and target nuclei, while NLDs indicate the number of accessible energy states within a nucleus. By integrating fresh data, researchers can enhance the accuracy of nuclear reaction predictions, thereby reducing uncertainties and improving the reliability of models used in nuclear physics, astrophysics, and related technologies.

✠ ✠ ✠ ✠

References

[1] C. Iliadis (WILEY-VCH Verlag GmbH & Co. KGaA, 2007).

[2] C. E. Rolfs and W. S. Rodney (University of Chicago press, 1988).

[3] S. Woosley and W. Howard, Astrophysical Journal Supplement Series, vol. 36, Feb. 1978, p. 285-304. **36**, 285–304 (1978).

[4] D. L. Lambert, The Astronomy and Astrophysics Review **3**, 201–256 (1992).

[5] B. S. Meyer, Annual Review of Astronomy and Astrophysics **32**(1), 153–190 (1994).

[6] A. Palmisano-Kyle, A. Spyrou, P. DeYoung, et al., Physical Review C **105**(6), 065804 (2022).

[7] T. Rauscher, A. Heger, R. Hoffman, et al., The Astrophysical Journal **576**(1), 323 (2002).

[8] C. Travaglio, F. Röpke, R. Gallino, et al., The Astrophysical Journal **739**(2), 93 (2011).

[9] C. Travaglio, T. Rauscher, A. Heger, et al., The Astrophysical Journal **854**(1), 18 (2018).

[10] M. Kostur, M. Schindler, P. Talkner, et al., Physical review letters **96**(1), 014502 (2006).

[11] T. Rauscher, N. Dauphas, I. Dillmann, et al., Reports on Progress in Physics **76**(6), 066201 (2013).

[12] A. Koning, S. Hilaire, and M. Duijvestijn, NRG-1755 ZG Petten, The Netherlands (2019).

[13] V. Zerkin and B. Pritychenko, Nuclear Instruments and Methods in Physics Research Section A: Accelerators, Spectrometers, Detectors and Associated Equipment **888**, 31–43 (2018).

[14] T. Szücs, I. Dillmann, R. Plag, et al., Nuclear Data Sheets **120**, 191–193 (2014).

[15] A. Koning and J. Delaroche, Nuclear Physics A **713**(3-4), 231–310 (2003).

[16] A. Koning, S. Hilaire, and S. Goriely, Nuclear Physics A **810**(1-4), 13–76 (2008).

[17] R. Capote, D. L. Smith, and A. Trkov, in EPJ Web of Conferences, Vol. 8 (EDP Sciences, 2010), p. 04001.

[18] A. Koning, The European Physical Journal A **51**, 1–16 (2015).

[19] A. Koning and D. Rochman, Nuclear data sheets **113**(12), 2841–2934 (2012).

[20] M. Choudhary, A. Sharma, N. Singh, et al., Chinese Physics C **48**(9), 094104 (2024).

[21] A. Koning, S. Hilaire, and S. Goriely, The European Physical Journal A **59**(6), 131 (2023).

[22] T. Sauter and F. Käppeler, Physical Review C **55**(6), 3127 (1997).

[23] A. Sauerwein, M. Elvers, J. Endres, et al., Frontiers in Nuclear Structure, AstroPhysics, and Reactions: Finustar 3 **1377**, 423–425 (2011).

[24] J. Mayer, S. Goriely, L. Netterdon, et al., Physical Review C **93**(4), 045809 (2016).

[25] V. Foteinou, M. Axiotis, S. Harissopulos, et al., The European Physical Journal A **55**(5), 67 (2019).

[26] V. Foteinou, S. Harissopulos, M. Axiotis, et al., Physical Review C **97**(3), 035806 (2018).

[27] Y. Skakun, S. Utenkov, V. Mishchenko, et al., edited by I. M. Vyshnevskij, Ukraine, June 2010.

[28] G. Gyürky, Z. Fülöp, E. Somorjai, et al., Physical Review C **68**(5), 055803 (2003).

[29] G. Krivonosov, O. Ekhichev, B. Nemashkalo, et al., Journal of Izv. Rossiiskoi Akademii Nauk, Ser. Fiz **41**(10), 2196 (1977).

[30] https://www-nds.iaea.org/exfor/, Accessed: 2022-11-08, 2022.

[31] A. Hingu, P. Prajapati, S. Mukherjee, et al., in EPJ Web of Conferences, Vol. 275 (EDP Sciences, 2023), p. 02006.

[32] A. Hingu, S. Mukherjee, S. Parashari, et al., Chinese Physics C **48**(2), 024001 (2024).

[33] A. Hingu, B. Soni, S. Parashari, et al., Radiation Physics and Chemistry **199**, 110270 (2022).

[34] A. Hingu, S. Parashari, S. K. Singh, et al., Radiation Physics and Chemistry **188**, 109634 (2021).

[35] R. Debuyst and A. Vander Stricht, Journal of Inorganic and Nuclear Chemistry **30**(3), 691–698 (1968).